

Intersubband excitations in ultrathin core-shell nanowires in the one-dimensional quantum limit probed by resonant inelastic light scattering


Sebastian Meier,¹ Paulo E. Faria Junior,² Ferdinand Haas,¹ Emma-Sophia Heller,¹ Florian Dirnberger,³ Viola Zeller,¹ Tobias Korn,⁴ Jaroslav Fabian,² Dominique Bougeard,¹ and Christian Schüller¹

¹*Institut für Experimentelle und Angewandte Physik, Universität Regensburg, D-93040 Regensburg, Germany*

²*Institut für Theoretische Physik, Universität Regensburg, D-93040 Regensburg, Germany*

³*Department of Physics, City College of New York, New York 10031, USA*

⁴*Institut für Physik, Universität Rostock, D-18059 Rostock, Germany*

 (Received 20 September 2021; revised 4 December 2021; accepted 7 December 2021; published 22 December 2021)

We investigate single, ultrathin, pure-wurtzite-phase GaAs-AlGaAs core-shell nanowires by resonant inelastic light scattering (RILS). We observe electronic Raman excitations, which can be attributed to intersubband excitations of photoexcited electrons or holes within the quasi-one-dimensional (1D) subband structure. Our analysis reveals that the electronic systems in the narrowest investigated nanowires, with GaAs core diameters down to 25 nm, are in the 1D quantum limit. Excitation-density-dependent measurements indicate that the observed 1D intersubband excitations are mainly of single-particle origin, since no plasmonic shift can be deduced. Our experimental findings are consistent with a three-step scattering mechanism, based on the Coulomb interaction of photoexcited electron-hole pairs with free carriers, electrons, or holes. The quantized subband energies, as extracted from photoluminescence, photoluminescence-excitation, and RILS experiments, can be nicely reproduced by realistic multiband $\mathbf{k} \cdot \mathbf{p}$ band structure calculations, taking into account the hexagonal geometry of the nanowires.

DOI: [10.1103/PhysRevB.104.235307](https://doi.org/10.1103/PhysRevB.104.235307)

I. INTRODUCTION

Low-dimensional semiconductors represent a powerful testbed to explore quantum confinement and its effects on the interactions between quasiparticles. In this endeavor, semiconductor heteroepitaxy alongside van der Waals two-dimensional (2D) crystals has enabled numerous experimental studies of quasiparticle excitations and their interactions in quasi-zero-dimensional (0D) and 2D systems. In contrast to that, implementations of quasi-one-dimensional (1D) systems in the quantum limit allowing one to study such interactions are rare and only a few of them readily accessible in experiments. Very recently, the demonstration of self-assembled growth of ultrathin GaAs-based nanowires [1–4] has opened the perspective to investigate 2D quantum confinement effects in 1D structures with unprecedentedly high confinement energies in optical spectroscopy.

Resonant inelastic light scattering (RILS)—also called electronic Raman scattering—has proven over decades to be a very powerful tool for the investigation of electronic excitations in semiconductor nanostructures, based on zincblende-type materials, like the GaAs-AlGaAs or InAs-InGaAs system (for an overview, see [5]). The seminal pioneering works in this area were the first experimental observations of intersubband excitations in modulation-doped GaAs-AlGaAs quantum wells by Pinczuk *et al.* [6] and in GaAs-AlGaAs heterojunctions by Abstreiter *et al.* [7]. In the following decades, also experiments on lower-dimensional systems, 1D quantum wires [8–19], and 0D quantum dots [10,20–24] were reported. Most of those experiments were performed on lithographically defined samples with typical lateral dimensions

on the order of 100 nm, or, later, on self-assembled InGaAs quantum dots [23,24]. In lithographically defined quantum-wire and quantum-dot systems, the quantization energies are typically on the order of one or only a few meV. In such systems, typically a significant number of states are occupied in modulation-doped structures. The strength of the RILS method lies in the possibility to discriminate between different types of electronic excitations via polarization selection rules. In the literature, three types of electronic excitations are discussed, which can be probed via RILS, which are spin-density excitations (SDEs), charge-density excitations (CDEs), and single-particle excitations (SPEs). The first two types can be unambiguously identified via polarization selection rules: SDEs are observed for perpendicular linear polarizations of the incident and scattered light, while CDEs are active for parallel linear polarizations [25]. SPEs, on the other hand, are reported for both polarization configurations, i.e., they do not seem to obey particular polarization selection rules [26]. SDEs and CDEs are collective excitations of electrons, i.e., coherent plasma oscillations. CDEs (plasmons) are blueshifted with respect to excitations of a noninteracting electron system, due to the direct, repulsive Coulomb interaction, while SDEs show a redshift due to the attractive exchange Coulomb interaction. SPEs, which, by definition, have energies close to excitation energies of noninteracting electrons were controversially discussed in literature. It was experimentally found that they dominate under conditions of extreme resonance [10], when the energy of the exciting laser is close to the band gap of the material. For GaAs-AlGaAs quantum wires and quantum dots it has been experimentally shown that under such

conditions of extreme resonance unpolarized SPEs can be observed, while at laser energies above the fundamental band gap, collective SDEs and CDEs can be found with the established polarization selection rules [10]. For quantum dots [27] and quantum wires [28] this was confirmed afterwards by model calculations, where the electronic excitations are included in the framework of the random-phase approximation, and the resonant valence- to conduction-band transitions are included in the formalism. This was later also shown for quantum wells [29]. A reasonable explanation for the presence of unscreened SPEs is that in the collective excitations the electron plasma oscillates coherently, while SPEs consist of incoherent electron oscillations, where interaction effects, at least partially, cancel out [27,30,31]. This has been shown on a quantitative level by exact diagonalization calculations for few-electron quantum dots [30].

All the experimental works cited above were performed on large arrays, i.e., large numbers of wires or dots. The recent availability of ultrathin GaAs-AlGaAs core-shell nanowires [1–4] now makes single wire spectroscopy of strong confinement in 1D structures accessible. So far, however, there are no reports about the investigation of *electronic* excitations of 1D charge-carrier systems in nanowires available. Raman investigations on nanowires with diameters on the order of 100 nm have focused so far on the investigation of phonons [32–36].

In this work we present RILS experiments on single core-shell nanowires with very narrow GaAs core diameters down to 25 nm. We observe electron and hole intersubband excitations of the photoexcited 1D electron-hole plasma, which can be understood by 2D quantum-confinement effects of the 1D structures, which are on the order of tens of meV for the narrowest nanowire. From density-dependent experiments we infer that the 1D intersubband excitations are predominantly of single-particle type. We propose a three-step scattering mechanism, based on the Coulomb interaction between photoexcited electron-hole pairs and the electron-hole plasma, which can explain the most salient features of our experimental results. The energetic subband structure, as experimentally deduced from RILS, photoluminescence, and photoluminescence-excitation experiments, is well described by results of realistic $\mathbf{k}\cdot\mathbf{p}$ model calculations.

II. EXPERIMENTAL AND THEORETICAL DETAILS

Nanowire samples. Pure wurtzite-phase GaAs-AlGaAs core-shell nanowires are grown by the vapor-liquid-solid (VLS) growth method in a molecular-beam epitaxy system [1]. The GaAs nanowire core is covered with a nominally 15-nm-thick $\text{Al}_{0.32}\text{Ga}_{0.68}\text{As}$ shell to avoid nonradiative recombination at the GaAs surface. A 7.5-nm-thick GaAs cap layer protects the AlGaAs layer from oxidation. All nanowires are undoped. Transmission and scanning electron microscopy investigations show that the wires have a hexagonal cross section and crystallize in the wurtzite crystal phase [37,38]. In this work, wires from three different growth runs, with average GaAs core diameters of 25 nm, 40 nm, and 50 nm, are investigated. Experiments on three selected single wires with core diameters of 25 nm, 31 nm, and 41 nm are exemplarily

presented and discussed. The exact core diameters are determined by comparison of the experimentally extracted subband energies to model calculations (see further below). For the nominally 40-nm wire (50-nm wire) this has led to a correction of the diameter to 31 nm (41 nm), which is within the experimentally observed average diameter distribution range. For the 25-nm wire, the nominal diameter is confirmed by the experimental and theoretical analysis. Figure 1(b) shows a scanning-electron micrograph of an as-grown single wire out of the 25-nm-core-diameter growth run. Note that this wire also contains the AlGaAs shell and the cap layer. Its total diameter is therefore larger than 25 nm. For the optical experiments, the wires are broken off the growth substrate in an ultrasonic bath. The liquid containing the wires is then dropped onto an oxidized silicon substrate, resulting in few-micron-long wires, lying horizontally on the silicon-dioxide surface, with average distances between individual wires, which allow for the investigation of single wires via optical microscopy. In Fig. 1(a), a dark-field microscope image of such a sample is displayed. The dashed green circle marks for clarity a single nanowire, which can be addressed by a focused laser beam.

Optical experiments. For the optical experiments, the sample is mounted in a cold-finger microscope cryostat and is kept at a nominal temperature of about $T = 4$ K. The beam of a tunable continuous-wave Ti:sapphire laser is focused with a $100\times$ microscope objective onto the sample, resulting in a spot diameter of about $2\ \mu\text{m}$. Raman and photoluminescence (PL) spectra of single nanowires are recorded with a triple Raman spectrometer in subtractive mode, equipped with a liquid-nitrogen-cooled charge-coupled-device camera. Linear polarizers are used to define the polarization directions of the incoming and scattered light. Figure 1(c) is a schematic picture of the scattering geometry. The laser beam is perpendicular to the nanowire and focused by a microscope objective, which also collects the backscattered light. Due to the numerical aperture of 0.8 of the objective, a distribution of finite wave vectors q is transferred parallel to the wire axis. Since the wavelength λ of the incident and that of the inelastically scattered light are approximately equal, the maximum value in z direction is given by $q_z \sim 4\pi/\lambda \times 0.8$. In the RILS spectra displayed below, the scattering geometries are denoted by the Porto notation $a(c, d)b$, where a and b give the propagation directions and c and d the linear polarization directions of the incoming and scattered light. The RILS experiments are taken with a laser power of $50\ \mu\text{W}$ if not otherwise noted. As will be shown in the main body of the manuscript, for this illumination density, the density of photoexcited electron-hole pairs in the nanowires is on the order of $1 \times 10^6\ \text{cm}^{-1}$. Since the Mott density for GaAs nanowires is at about $3 \times 10^5\ \text{cm}^{-1}$ [39], we assume that excitonic effects are of minor importance for our experiments. In most of the experiments we rather excite an electron-hole plasma of free carriers with equal densities of electrons and holes.

For the photoluminescence-excitation (PLE) experiments, the intensity of the fundamental PL is recorded in dependence of the photon energy of the exciting laser. As long as nonradiative relaxation channels are of minor importance, the PLE spectrum approximates the absorption spectrum of the sample.

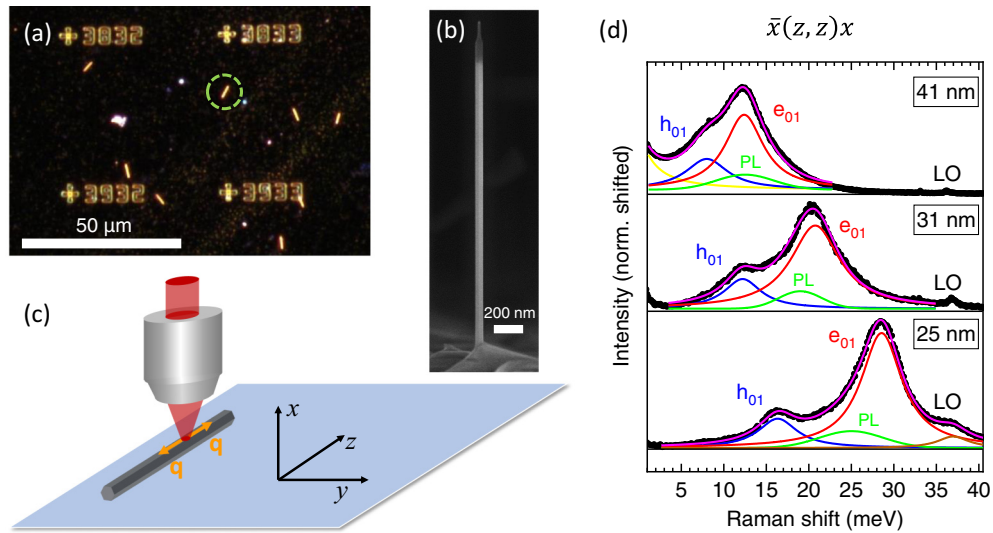


FIG. 1. (a) Microscope image of a sample, where nanowires are deposited on a silicon-silicon dioxide wafer. The green dashed circle marks a single nanowire. The golden numbers and crosses are for orientation on the sample. (b) Scanning-electron micrograph of an as-grown nanowire, before it is broken off in an ultrasonic bath. (c) Schematic picture of the experimental setup for the Raman and PL experiments. Wave vectors q , which are transferred to the nanowire because of the final aperture of 0.8 of the microscope objective, are indicated. The coordinate system, used to define the scattering geometries, is also shown. (d) Resonant inelastic light-scattering spectra of three different single nanowires with GaAs core diameters of 41 nm, 31 nm, and 25 nm, taken at laser energies of 1640 meV, 1647 meV, and 1664 meV, respectively, close to the resonance maxima of e_{01} . The solid lines are results of fits with Lorentzian lines, except for the green lines, which are Gaussians. The magenta line is the sum of all fit curves. The green curve describes a hot PL line to the light-hole band. The yellow line corresponds to stray light from the laser. The scattering geometry is given in the figure.

Theoretical modeling. The band structure calculations for the GaAs nanowires are performed using the $\mathbf{k} \cdot \mathbf{p}$ method combined with the envelope function approximation. This technique allows us to incorporate the spatial dependence of the intrinsic parameters and to model the hexagonal quantum confinement of the nanowire [40–43]. The set of coupled differential equations in real space are solved numerically using the plane-wave expansion, i.e., the spatial dependence of wave functions, parameters, and potentials is expanded in Fourier coefficients [44–47]. Specifically for the GaAs wurtzite low-energy bands, we use the six-band $\mathbf{k} \cdot \mathbf{p}$ model for the valence band (which incorporates the heavy hole, light hole, and crystal-field split-off hole) and the conduction band is treated within the parabolic model with distinct effective masses for in-plane (perpendicular to the [0001] axis) and out-of-plane (parallel to the [0001] axis) directions. For further details on the $\mathbf{k} \cdot \mathbf{p}$ model and specific definition of parameters please refer to Refs. [48–50]. The valence band parameters and the electron effective masses for GaAs wurtzite are taken from Ref. [49] (GW-LDA data set, neglecting the spin splitting in the valence band since wurtzite nanowires with [0001] growth direction do not exhibit any spin splitting [51]). For the numerical solution of the nanowire we considered 20 plane waves along x and y directions on a square grid, leading to 41×41 Fourier coefficients for the wave functions and 81×81 for the parameters and potentials. Additional details of this methodology applied to semiconductor nanowires can be found in Refs. [1,51]. For the calculation of the absorption spectra [52], we considered 1001 k -points (k_z) and introduced a Lorentzian broadening with a full width at half maximum of 2 meV to obtain a smooth absorption curve. The different contributions of the light polarization parallel and perpendicu-

lar to the nanowire growth direction are direct manifestations of the intrinsic optical selection rules of wurtzite materials [48,53], embedded in the particular composition of heavy, light, and crystal-field split-off bands. Furthermore, since interband Kane parameters in GaAs wurtzite are not well established [54] and we are mainly interested in the energetic position of the absorption peaks, we have considered $P_1 = P_2$ in the calculated absorption spectra, with P_1 (P_2) being the amplitude of the dipole matrix element for out-of-plane (in-plane) light polarization.

III. RESULTS AND DISCUSSION

We start by comparing RILS spectra of three different single nanowires, which were taken from three growth runs with nominal GaAs core diameters of 25 nm, 40 nm, and 50 nm. Figure 1(d) displays RILS spectra of the three selected single wires, recorded in $\bar{x}(z, z)x$ scattering geometry. In the following we use the simplified notation e_i , h_i , and l_i for the 1D electron, heavy-, and light-hole subbands, respectively. The indices $i = 0, 1, 2, \dots$ are used to order the states with increasing energy. Very small energy splittings of some of the states, due to the anisotropic symmetry of the hexagonal cross section of the wires, are omitted for the moment. We will come back to these below when discussing the calculated band structure. To avoid the strong PL background from the fundamental band gap PL in the RILS spectra, the laser energies are chosen to be close to light-hole to conduction-band transitions of the corresponding wires, i.e., about 100 meV above the fundamental band gap transition $h_0 \rightarrow e_0$. The exact laser energies are given in the caption of Fig. 1. The experimental spectra are shown in Fig. 1(d) by black dots, while the

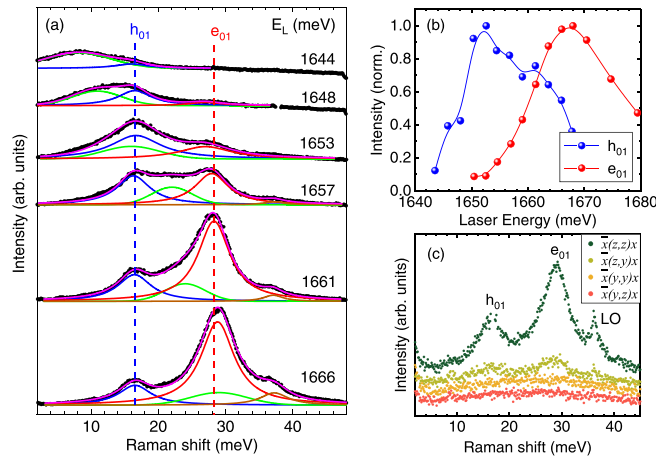


FIG. 2. (a) Series of RILS spectra, taken in $\bar{x}(z, z)x$ scattering geometry, for different laser energies, as given in the figure. The solid colored lines are fit results, using a set of Lorentzian lines, except for the green lines, which are Gaussians. The magenta lines are the respective sum of all fit curves. (b) Intensities of the h_{01} and e_{01} Raman excitations versus laser energy. (c) Comparison of RILS spectra for different scattering geometries, as indicated in the figure. The spectra are recorded at a laser energy of 1664 meV.

colored lines are results of fits, using a set of Lorentzian lines, except for the green lines (hot PL), which are Gaussian lines. The magenta lines represent the sums of the corresponding single lines. Besides the longitudinal optical (LO) phonon of GaAs, two prominent Raman excitations can be identified in each spectrum (blue and red fit curves), where the energies of the excitations increase with decreasing wire diameter. We interpret the two excitations as intersubband excitations of (i) photoexcited electrons from the 1D electronic ground state e_0 to the first excited state e_1 in the conduction band, $e_0 \rightarrow e_1$, labeled as e_{01} in Fig. 1(d), and (ii) of photoexcited holes from the ground-state heavy-hole subband to the first excited heavy-hole subband, $h_0 \rightarrow h_1$, labeled as h_{01} in Fig. 1(d). This identification is strongly supported by the good coincidence of the transition energies with results of our realistic $\mathbf{k} \cdot \mathbf{p}$ band structure calculations [see Figs. 5(a) and 5(b), for 25 nm and 31 nm nanowires, respectively]. The green solid lines in Fig. 1(d) describe hot PL recombinations, resulting from dipole-allowed resonant $e_0 \rightarrow l_0$ transitions at the 1D van Hove singularity. To verify that the observed intersubband excitations e_{01} and h_{01} are indeed Raman excitations and not due to hot PL, we show exemplarily in Fig. 2(a) a selection of RILS spectra of the 25-nm nanowire for different laser energies. As can be seen in the figure by the vertical dashed lines, the Raman shifts of e_{01} and h_{01} are independent of the laser energy, while the energy of the hot PL [green solid lines in Fig. 2(a)] stays approximately constant on an absolute energy scale at about 1635 meV, which is close to the $e_0 \rightarrow l_0$ transition energy of the 25-nm wire [cf. Fig. 6(a)]. From the other two nanowires we get similar results (not shown).

Figure 2(b) shows the resonance profiles of the two excitations, i.e., their intensities versus laser energy. The onsets of the resonances are shifted by ~ 12 meV, which matches the difference in excitation energies of ~ 28 meV for e_{01}

and ~ 16 meV for h_{01} . From that it follows that the resonant intermediate state in the scattering process is the same for both excitations, which is the $e_0 - l_0$ electron-hole pair (or exciton). This is further corroborated by the polarization characteristics of the scattering processes. Figure 2(c) shows a comparison of different scattering configurations, using linear polarizations of the incident and scattered photons, which are either parallel or perpendicular to the nanowire axis. Clearly, the signal is well pronounced for $\bar{x}(z, z)x$, only. It is well known for GaAs nanowires that transitions from heavy-hole states have a transition dipole, which is dominantly perpendicular to the wire axis (x and y directions), while the $l_0 \rightarrow e_0$ light-hole transition dominates for polarization parallel to the wire [cf. also band structure calculations in Figs. 5(a) and 5(b)]. Hence the observed polarization dependence of the Raman excitations underlines that, in the presented experiments, initially $l_0 - e_0$ electron-hole pairs are created and heavy-hole contributions are of minor importance.

Based on the experimental observations presented above, we propose a three-step, third-order scattering process for RILS on electron and hole intersubband excitations in the nanowires, which is based on the Coulomb interaction between photoexcited electron-hole pairs and charge carriers of the electron-hole plasma. Figure 3(a) is a schematic picture of the scattering process for creation of an e_{01} intersubband excitation in the conduction band. In the first step, an electron from the l_0 light-hole subband is excited into a virtual state close to the e_1 subband. The electron is then, in the second step, resonantly scattered into the e_0 subband via Coulomb interaction with another electron, which is already present in the e_0 subband due to photoexcitation. For energy conservation, the second electron is scattered at the same time from e_0 to e_1 , i.e., an e_{01} intersubband excitation is created. In the third step, the scattered electron-hole pair $e_0 - l_0$ at the van Hove singularity band edge recombines and emits the scattered photon. This means that—as observed in the experiments—the inelastically scattered light is resonant with the $e_0 \rightarrow l_0$ van Hove singularity hot PL for the case of extreme resonance. In Fig. 3(b), the corresponding process for the scattering by h_{01} heavy-hole intersubband excitations is illustrated. Photoexcited holes relax very quickly, on a subpicosecond timescale [55], to the bottom of the heavy-hole subbands and form there a photoexcited hole plasma. If the electron in step one is excited from l_0 into a virtual state, which is just by the energy of h_{01} above the e_0 subband, it can be resonantly scattered in the second step via Coulomb interaction with a hole in h_0 into the e_0 subband, and, at the same time, a h_{01} intersubband hole excitation is created in the valence band. Both scattering processes are consistent with the experimental observation that—for the resonant case—the energy of the scattered light is resonant with the $e_0 \rightarrow l_0$ van Hove singularity hot PL. This means that both scattering processes—for e_{01} as well as for h_{01} —are outgoing resonances. This is strongly corroborated by a comparison of the observed resonance energy to the calculated absorption (see discussion of Fig. 6 below).

The third-order matrix elements for the processes, displayed in Figs. 3(a) and 3(b), are given by [56, 57]

$$M = \sum_{v, v'} \frac{\langle f | \mathbf{A}_s \cdot \hat{\mathbf{p}} | v' \rangle \langle v' | \hat{V}_C | v \rangle \langle v | \mathbf{A}_i \cdot \hat{\mathbf{p}} | i \rangle}{(\hbar\omega_2 - E_{v'}) (\hbar\omega_1 - E_v)}. \quad (1)$$

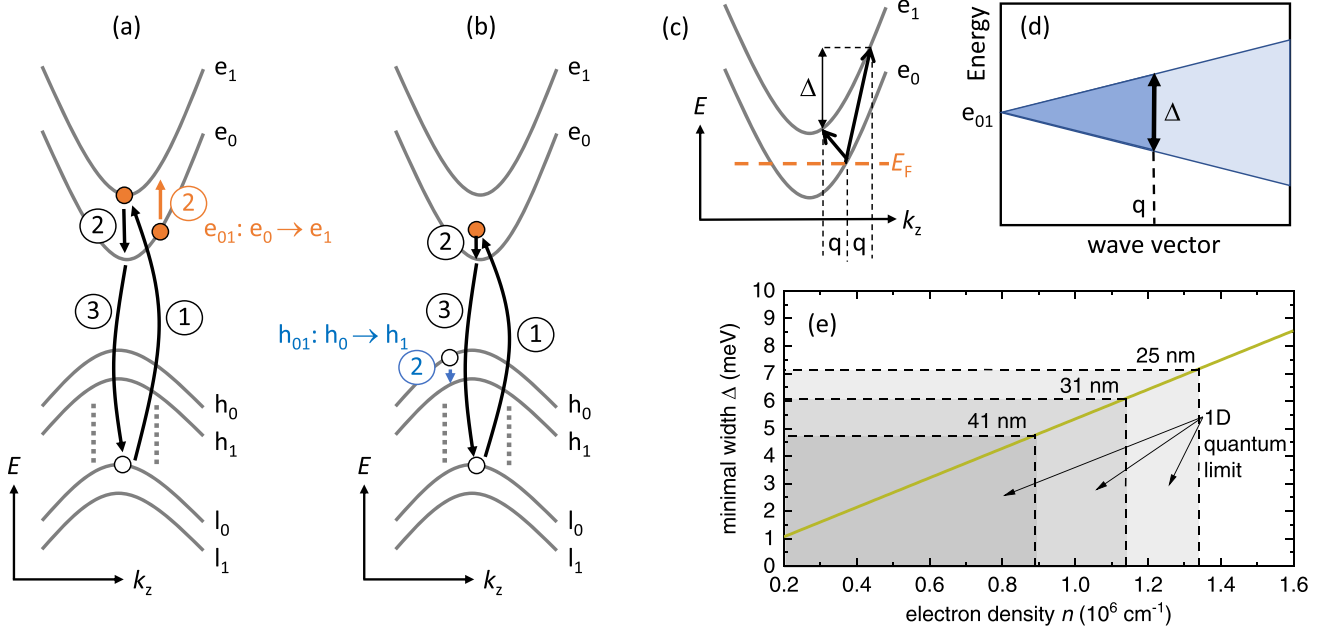


FIG. 3. (a) Schematic picture of a three-step scattering process for creation of an e_{01} intersubband excitation. In the first step an electron is excited from l_0 to a virtual state; in the second step the electron is scattered by Coulomb interaction with a photoexcited electron to e_0 , while the photoexcited electron is excited from e_0 to e_1 , i.e., an $e_0 \rightarrow e_1$ intersubband excitation is created. In the third step, the electron in e_0 recombines with the hole in l_0 . (b) Same as (a) but for the creation of a $h_0 \rightarrow h_1$ hole intersubband excitation. (c) Illustration of the maximum energetic width Δ of an intersubband excitation with finite momentum distribution q . (d) Schematic picture of the e_{01} single-particle continuum. All energies in the dark-blue shaded region contribute to the e_{01} intersubband excitation. (e) Maximum width Δ of the e_{01} intersubband excitation versus 1D electron density, calculated under the assumption that only the lowest subband is occupied. The gray-shaded regions indicate the density ranges, where wires with 25 nm, 31 nm, and 41 nm diameter are in the 1D quantum limit.

Here, $|i\rangle$ and $|f\rangle$ denote the initial and final states of the system, respectively. The initial state is the unperturbed photoexcited electron-hole plasma, while the final state may contain, in addition, an intersubband single-particle electron or hole excitation, e_{01} or h_{01} . $|\nu\rangle$ and $|\nu'\rangle$ are the first and second intermediate states with energies E_ν and $E_{\nu'}$. \mathbf{A}_i (\mathbf{A}_s) is the vector potential of the incident (scattered) photon and $\hat{\mathbf{p}}$ is the momentum operator. The matrix element in the middle describes the scattering from intermediate state $|\nu\rangle$ to $|\nu'\rangle$ via Coulomb interaction \hat{V}_C with the electron-hole plasma, where an intersubband excitation is created in the electron or hole system. The energy denominator becomes zero if either the energy of the electron-hole pair in the first intermediate state E_ν is a real state of the system and equal to the energy $\hbar\omega_1$ of the incident photon or if the scattered photon energy $\hbar\omega_2$ equals the energy $E_{\nu'}$ of an electron-hole pair in a real state. The latter is the case for the above-discussed processes. There, $E_{\nu'}$ is equal to the energy of the $e_0 - l_0$ electron-hole pair at the van Hove singularity. This leads to a strong resonance enhancement of the scattering process. For simplicity, the schematic diagrams in Figs. 3(a) and 3(b) are drawn for vertical transitions, neglecting a wave-vector transfer q_z in wire direction. Of course, similar processes also apply, taking into account the finite momentum transfer q_z .

We note that the proposed scattering process is similar to resonant Raman scattering by optical phonons in semiconductors, where the interaction term is the electron-phonon interaction. It is also similar to a three-step excitonic scatter-

ing process, suggested in 1989 by Danan *et al.* [56] for RILS on collective intersubband excitations and, later, by Govorov [57] on intrasubband excitations in GaAs quantum wells. Very recently, a related process was also suggested for RILS experiments on semiconducting carbon nanotubes, where excitons are created by inelastic light scattering [58].

All experiments presented so far are recorded with a laser power of $50 \mu\text{W}$. However, due to the different wire diameters and, hence, different active areas of the wires, and due to different absorption strengths [59], the electron/hole densities are expected to be different for the different wires at the same excitation power. Moreover, so far we have no information about the number of occupied electron and hole subbands in the experiments. To get a first handle on this, we evaluate in more detail the experimental linewidths of the observed intersubband excitations. We start by estimating the intrinsic upper limit for the linewidths in the 1D quantum limit. Figure 3(c) illustrates for a given occupation of the e_0 subband the two extreme cases of e_{01} intersubband excitations with maximum wave-vector transfer $q = q_z$, due to the finite aperture of the microscope objective [cf. Fig. 1(c)]. This leads to a maximum energy broadening of the e_{01} excitation of $\Delta \approx 2\hbar^2 k_F q_z / m^*$, where k_F is the magnitude of the Fermi wave vector and m^* the effective electron mass. For 1D systems, k_F and the electron density n are related by $k_F = n\pi/2$. Figure 3(d) displays schematically the single-particle continuum for e_{01} intersubband excitations under the assumption that only the lowest subband is occupied, i.e., that the electron system is in the 1D

quantum limit. All excitations which contribute to e_{01} due to the finite wave-vector distribution are highlighted by a darker blue shading. The maximum width is labeled by Δ . From the above considerations it follows that $\Delta \propto n$ in the 1D quantum limit. This proportionality is quantitatively shown in Fig. 3(e) by the green line, using an electron effective mass of $0.06m_0$ for the Γ_7 conduction band [49]. The different gray-shaded boxes indicate the density ranges, where nanowires of 25 nm, 31 nm, or 41 nm widths would be in the 1D quantum limit. We can also read off from this graph the corresponding maximum intrinsic widths Δ of the e_{01} intersubband excitation for the three cases. Since we expect in the realistic system an inhomogeneous broadening due to, e.g., diameter fluctuations of the nanowire within the illuminated lengths of $\sim 2 \mu\text{m}$, Δ represents the lower limit, expected for the experimentally observed excitation. From the spectra in Fig. 1(d) we can extract linewidths of the e_{01} excitation of about 5.8 meV for the 25-nm wire, 7.0 meV for the 31-nm wire, and of about 5.5 meV for the 41-nm wire. Comparing this to Fig. 3(e) we find that the linewidth for the 25-nm wire is with 5.8 meV well within the range of the 1D quantum limit. Quantitatively, we can read off an electron density of $1.1 \times 10^6 \text{ cm}^{-3}$ for this case, which would approximate the density if there would be no inhomogeneous broadening. Since we expect also a contribution to the linewidths due to inhomogeneous broadening, it follows that $n < 1.1 \times 10^6 \text{ cm}^{-3}$ for the 25-nm wire. Further below we will retrieve quantitative values for the electron densities via excitation-density-dependent measurements. However, so far we can definitely say that the 25-nm nanowire is in the 1D quantum limit. For the 31-nm wire we cannot be sure, since with about 7.0 meV the linewidth is just above the range of the 1D quantum limit for this wire width in the intrinsic case. Here it depends on the amount of inhomogeneous broadening whether or not this wire is in the 1D quantum limit. Again, below it will be shown that also this wire is in the 1D quantum limit. The same holds true for the 41-nm wire, where the observed linewidth is with about 5.5 meV also just above the intrinsic range.

Next, we investigate the excitation-density dependence of the signals. We focus in the remainder on the 25-nm and 31-nm wires, since there the quantization effects are most pronounced. The laser energy in these experiments is adjusted slightly above the resonance positions of e_{01} to get strong e_{01} and h_{01} Raman signals, and the $\bar{x}(z, z)x$ scattering geometry is used. Therefore, we can resonantly populate the first and the edge of the second electron subbands only. This means that, at sufficiently high laser powers, the total electron and hole densities may show some saturation effect and will not increase to arbitrarily large values because of Pauli blocking. Since the heavy-hole effective mass is with $m_h^* = 0.75m_0$ [49] twelve times larger than the electron effective mass, even when the second electron subband e_1 gets populated, only the lowest heavy-hole subband h_0 will be significantly occupied.

Figures 4(a) and 4(b) show RILS and PL spectra of the 31-nm wire for different laser intensities. Since for the density-dependent experiments a modified experimental setup was used in order to reach larger illumination powers, we evaluate in the following the laser powers relative to a power P_0 , which in the previous experiments would correspond to $P_0 = 50 \mu\text{W}$. We have adjusted this by the intensity ratio of

the h_{01} and e_{01} excitations in the spectra. In the PL spectra the emergence of the excited-state PL $e_1 \rightarrow h_1$ can be seen. While the RILS spectra are normalized and vertically shifted for better comparability, in Fig. 4(b), the raw data PL spectra are displayed. In Fig. 4(c), the intensity of the excited-state PL is plotted versus laser power. Via the black solid line, which is a linear fit to the data points, a zero intensity at about $1.2P_0$ can be estimated. From this we conclude that the population of the e_1 subband starts at this laser power. Taking into account the experimentally determined e_{01} energy of $\sim 21 \text{ meV}$ for the electron Fermi energy, this results in an electron density of $\sim 1.2 \times 10^6 \text{ cm}^{-3}$. From this we conclude that, in the experiments above with laser power P_0 , the density in the 31-nm wire is $\sim 1.0 \times 10^6 \text{ cm}^{-3}$, which is well within the 1D quantum limit [cf. Fig. 3(e)]. Furthermore, it follows that about 25% of the observed linewidth of 7 meV in Fig. 1(d) is resulting from inhomogeneous broadening. Next, we will have a closer look onto the density dependence of the Raman excitations in Fig. 4(a). The h_{01} intersubband hole excitation vanishes for laser powers $> P_0$. This can be understood as follows: the resonant scattering process, displayed in Fig. 3(b), is effective only as long as the electron Fermi energy in e_0 is smaller than the h_{01} excitation energy. Otherwise, the process is suppressed by Pauli blocking. This roughly coincides with our finding above that the electron Fermi energy reaches the e_1 electron subband at a laser power of about $1.2P_0$. Or, in other words, if we were not in the 1D quantum limit at a laser power of P_0 , we would not observe the h_{01} heavy-hole intersubband excitation, since its resonant scattering process would be blocked. The analogous experiments on the 25-nm wire are shown in Figs. 4(d) to 4(f). With a similar analysis we find here for the 25-nm wire an electron density of about $0.24 \times 10^6 \text{ cm}^{-3}$ for experiments with a laser power of P_0 . This density is close to the Mott density for GaAs nanowires [39]. Therefore, we cannot fully exclude the influence of excitonic effects on the intermediate states for this situation. Again, comparing with Fig. 3(e), this density is well within the 1D quantum limit for the 25-nm wire. Furthermore, comparing the “intrinsic” linewidth corresponding to this density from Fig. 3(e) to the experimentally observed one of $\sim 5.8 \text{ meV}$, we find that about 77% of the linewidth is caused by inhomogeneous broadening, which is significantly more than for the 31-nm wire. This seems reasonable, taking into account that, due to the $\sim 1/d^2$ dependence of the quantization energies on the diameter d of a nanowire, the influence of wire-width fluctuations on the linewidth becomes quantitatively more important the thinner a wire is [60].

We assume that the carrier system is mostly thermalized with the lattice in our experiments, due to the greatly enhanced lifetime of photoexcited electron-hole pairs in ultrathin nanowires, which goes up to several tens of ns [1,59]. This holds within the whole range of applied illumination densities. We infer this by comparison to temperature-dependent measurements of the electronic excitation e_{01} and h_{01} (not shown), which show that their intensities strongly decrease with increasing lattice temperature, and can no longer be observed for temperatures $> 40 \text{ K}$. In our density-dependent measurements at low temperature, presented in Figs. 4(a) and 4(d), on the other hand, we do not observe a significant saturation effect of the intensities of the electronic excitations

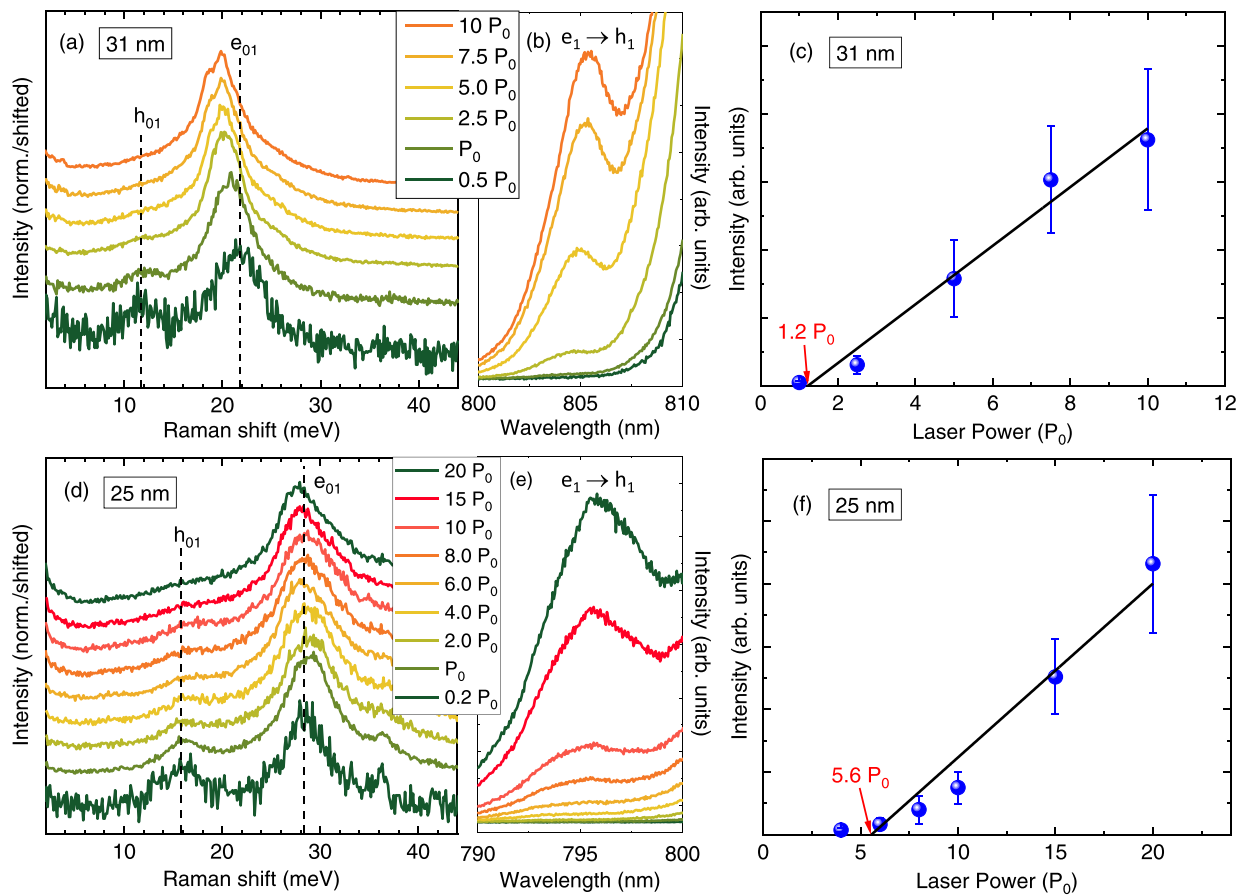


FIG. 4. (a) RILS spectra of the 31-nm wire for different laser powers, given relative to a power P_0 , which is equivalent to the power used in the experiments, displayed in Fig. 1(d). The spectra are normalized and vertically shifted for clarity. (b) PL spectra of the excited state PL $e_1 \rightarrow h_1$ for different laser powers. (c) Intensities of the $e_1 \rightarrow h_1$ PL line versus laser power. The black line is a linear fit to the data. The intersection with the x axis is given in red. (d)–(f) Same as (a)–(c) but for the 25-nm wire. The spectra in (a) and (b) are taken at a laser energy of 1646 meV and those in (d) and (e) at 1666 meV.

with increasing illumination power in the raw data; they rather increase in intensity with increasing illumination power. From this we conclude that within the measured density range the carrier system seems to be mostly thermalized with the lattice.

The density-dependent RILS experiments in Figs. 4(a) and 4(d) allow us to draw conclusions about the type of the observed electronic intersubband excitations. By the vertical dashed lines we can see that there is a slight redshift of the intersubband excitations with increasing laser power, i.e., with increasing electron and hole densities. This is much more pronounced for the 31-nm wire in Fig. 4(a), which has a larger effective area and almost by an order of magnitude larger densities, than for the 25-nm wire in Fig. 4(d). For collective charge-density excitations, i.e., intersubband plasmons, we would expect just the opposite: an increase of the energy with increasing density due to the repulsive Coulomb interaction. Collective spin-density excitations, on the other hand, would redshift with increasing carrier density. However, polarization selection rules, derived for zinc-blende-type semiconductors [25], dictate that spin-density excitations are allowed for crossed linear polarizations of incident and scattered photons only. The most obvious difference of the

wurtzite phase, in comparison to the zinc-blende phase, is that the heavy-light-hole degeneracy is lifted in the bulk crystal. Inspection of the selection rules on the basis of the wurtzite Kane model [48] reveals that in the wurtzite phase the selection rules for charge- and spin-density excitations are still valid in good approximation, since also there the Bloch functions are composed of s -like and p -like atomic functions in the conduction and valence band, respectively. Clearly, as shown in Fig. 2(c) above, in our experiments the Raman signals are dominant for parallel linear polarizations, where collective charge-density excitations and single-particle excitations are allowed. Furthermore, there is no depolarization shift detectable for crossed versus parallel linear polarization configurations [cf. Fig. 2(c)], which leads us to the assumption that we dominantly observe single-particle excitations.

There is another strong argument for the single-particle nature of the observed excitations, which is the lack of a significant plasmon-phonon coupling in the experiments. In polar GaAs there is usually a strong coupling of plasmons and the LO phonon via the macroscopic electric fields of both excitations, which can lead to significant energy shifts. This was first noticed in n -doped bulk GaAs by Mooradian and

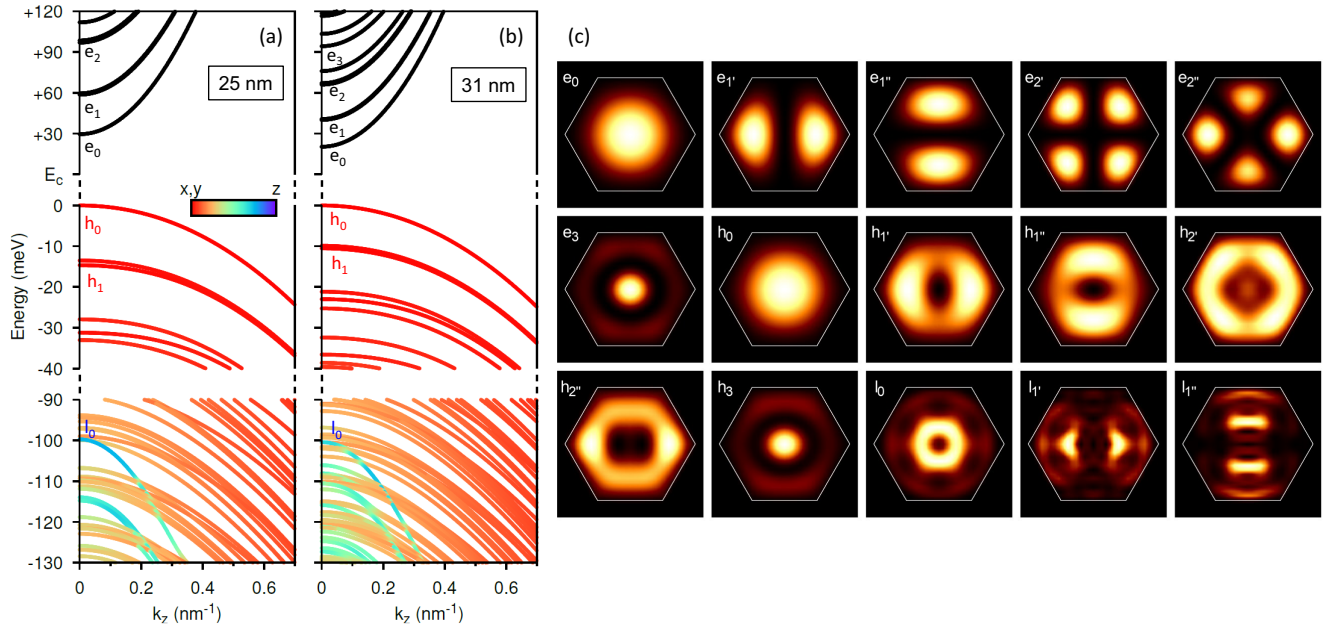


FIG. 5. (a) Results of a $\mathbf{k} \cdot \mathbf{p}$ subband calculation for a realistic hexagonal nanowire with 25 nm GaAs core diameter. The relevant electron-, heavy-, and light-hole states are labeled by e_n , h_n , and l_n , respectively. The color scale for the valence-band states indicates the polarization of the transition dipole to the conduction band due to the valence-band mixing effects. (b) Same as (a) but for 31 nm GaAs core diameter. (c) Plots of the probability density of some of the 1D subbands of the 25-nm wire. The bands, e.g., e_1 , e_2 , h_1 , h_2 , and l_1 , show a splitting due to the anisotropic symmetry of the hexagonal cross section, indicated by the labels ' and ''.

Wright [61], and is reported in many papers on modulation-doped quantum wells, e.g., in Refs. [6,56]. In Fig. 1(d), where we compare spectra of the three wires directly, one can see that the LO phonon is essentially unchanged in energy. For the 25-nm wire the energy e_{01} is closest to the LO phonon. There, the LO phonon seems to be broader, i.e., damped, in comparison to the other two wires, but not shifted in energy. The broadening could be due to Landau damping, i.e., the decay into uncorrelated electron-hole pairs, as also observed for the LO phonon in graphene [62]. The absence of a significant plasmon-phonon coupling effect in our experiments is, hence, an additional hint for the single-particle nature of the excitations. In summary, we conclude that an approximate treatment of the excitations as excitations of noninteracting particles, neglecting direct and exchange Coulomb-interaction effects, is appropriate. The origin of the slight redshift of e_{01} with increasing density, which is more pronounced for the 31-nm wire with the larger densities [cf. Fig. 4(a) vs 4(d)], is unclear at the moment. It may be an intricate property of interactions in the photoexcited electron-hole plasma (see also discussion of experiments at high illumination power further below).

In the following, we will briefly discuss the results of the $\mathbf{k} \cdot \mathbf{p}$ band structure calculations. Figures 5(a) and 5(b) show the calculated subband dispersions for the 25-nm and 31-nm nanowires, respectively. The energy scales show the calculated subband energies relative to a band gap energy E_c , which is adjusted below to the experiments. The color scale, used for the valence-band subbands, indicates the orientation of the transition dipole to the conduction band. One can see that heavy-hole transitions are dominant for light polarizations perpendicular to the wire (x, y directions), while for the light-

hole ground state l_0 , close to $k_z = 0$, the transition dipole has a strong z component. This is more pronounced for the 25-nm wire than for the 31-nm one. There, the light-hole transition represents a mixture of perpendicular and parallel components. Nevertheless, since the heavy-hole transitions have a clear perpendicular component, only in the scattering geometry $\bar{x}(z, z)x$, which is used in the RILS experiments light-hole transitions are excited predominantly. Figure 5(c) displays the calculated probability densities of selected 1D subbands at $k_z = 0$. The white hexagons outline the cross section of the GaAs region. The e_0 and h_0 ground states show an almost cylindrical symmetry. However, for the excited states e_1 , e_2 , h_1 , h_2 , and l_1 , the anisotropic symmetry of the hexagonal cross section leads to two slightly different configurations for the corresponding wave functions. For the e_1 state, e.g., these two configurations are labeled by e_1' and e_1'' in Fig. 5(c). The two different possibilities for the excited state wave functions lead to small splittings of the subbands, which are typically below 1 meV. In Fig. 5(a), this splitting is most pronounced for the h_1 subband. For most of the states, it can hardly be recognized within the used widths of the lines in Figs. 5(a) and 5(b). Also in the experiments we have no clear evidence for these splittings because of the experimental linewidths, which are on the order of several meV.

Now, we come to a central point of this work—the quantitative comparison of the experimental results to the calculated 1D subband structure. To this end, we plot in the upper parts of Figs. 6(a) and 6(b) calculated absorption spectra, based on the above-described band structure calculations. The red curves are the absorption for linear polarization perpendicular to the wires, while the blue curves are results for linear polarization parallel to the wires. The van Hove singulari-

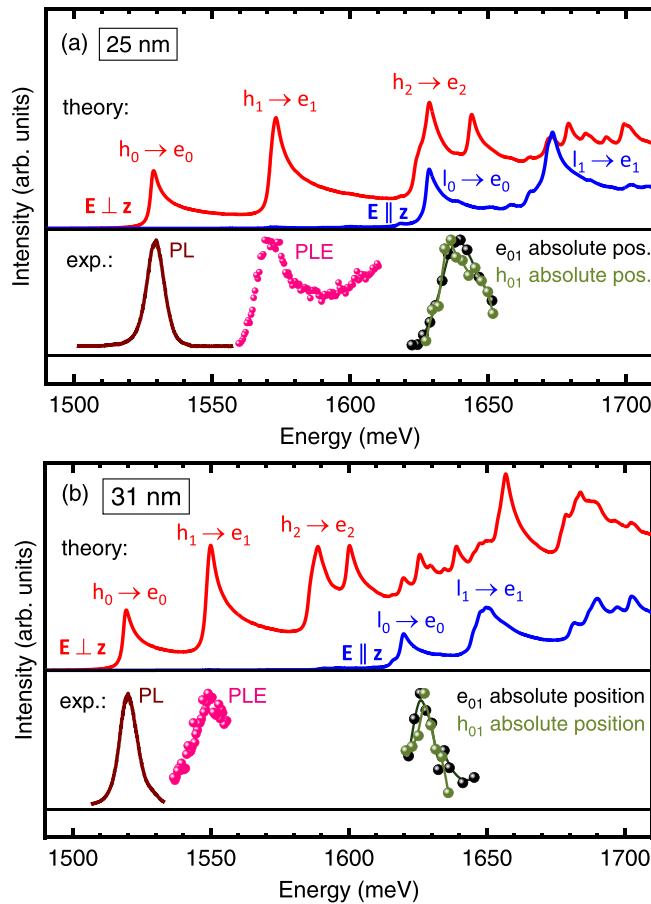


FIG. 6. (a) Comparison of calculated absorption spectra for the 25-nm nanowire (upper panel) to experimental results. (b) Same as (a) but for the 31-nm nanowire.

ties are labeled with the corresponding transitions, which are relevant for the comparison to the experiments. The brown curves in both figures are PL spectra with linear polarization perpendicular to the wires, corresponding to $e_0 \rightarrow h_0$ transitions. The calculated absorption spectra are rigidly shifted so that the $h_0 \rightarrow e_0$ transitions coincide with the measured PL positions. From this we receive values for the effective band gap E_c of 1496.5 meV and 1498.5 meV for the 25-nm and 31-nm wire, respectively. These values are roughly 20 meV smaller than the bulk band gap energy of undoped wurtzite-type GaAs, which is about 1520 meV. We believe that the reason for this is the band gap renormalization effect due to the photoexcited electron-hole plasma in the wires. As shown above, for nominally the same excitation powers, different densities are excited in the two wires due to their different widths. Therefore, it is not surprising that the two values for E_c are not identical. The magenta dots display PLE measurements with $\bar{x}(y, y)x$ polarization configuration, exciting and detecting dominantly heavy-hole transitions. The PLE measurements for both wires are averaged over up to five measurements. It was only possible to get reasonable PLE spectra in the displayed energy range. As elaborated above, the second intermediate state in the RILS experiments on e_{01} and h_{01} intersubband excitations is the $e_0 - l_0$ electron-hole pair. Therefore, we have plotted in Figs. 6(a) and 6(b) the

intensities of the two Raman excitations versus energy of the scattered light, i.e., versus the absolute resonance position. If our interpretation of the Raman processes is correct, this should follow the absorption at the $l_0 \rightarrow e_0$ van Hove singularity. One can recognize in Figs. 6(a) and 6(b) that for both Raman excitations in both nanowires this is reasonably well fulfilled [green and black dots in Figs. 6(a) and 6(b)]. Using the crystal field and spin-orbit coupling parameters of Ref. [49], the calculated heavy-light hole splitting for bulk GaAs amounts to ~ 102 meV. This value is consistent with other theoretical studies [63–65] and experimental reports [2,32,66,67] suggesting that the heavy-light hole splitting is ~ 100 meV. Furthermore, the energy difference between the ground-state PL $e_0 \rightarrow h_0$ and the excited-state PLE transition $h_1 \rightarrow e_1$ should just be equal to the sum of the e_{01} and h_{01} transition energies. This is nicely verified in our experiments with ~ 45 meV (~ 33 meV) for the sum of the e_{01} and h_{01} transition energies for the 25-nm (31-nm) wire, which underlines our interpretation that the observed intersubband excitations are mainly of single-particle origin. In summary, the results of PL, PLE, and RILS experiments on electron and hole intersubband excitations confirm nicely the calculated subband structure of the ultrathin nanowires.

Finally, in the last part of this work, experiments with high illumination power of 5 mW will be discussed, where the second 1D electron subband is significantly populated. This was only possible for the 31-nm wire. Only in this wire we could detect also intersubband excitations, starting from the second electron subband e_1 . The reason for this may be that due to the larger effective area of this wire, and the smaller subband quantization energies in comparison to the 25-nm wire, this regime could conveniently be reached. Figure 7(a) shows a series of RILS spectra of the 31-nm nanowire for different laser energies, recorded in $\bar{x}(z, z)x$ scattering geometry. At this high excitation power, the h_{01} intersubband excitation is already strongly quenched due to Pauli blocking, and the e_{01} electron intersubband excitation shows a significant redshift of about 3 meV in comparison to the above experiments at 50 μ W, where the wire is in the 1D quantum limit. At larger laser energies two additional Raman excitations appear, which we interpret as e_{12} and e_{13} intersubband excitations, starting at the second electron subband e_1 . Also these excitations, which can be observed in Fig. 7(a) at about 22 meV and 29 meV, are redshifted in comparison to the subband calculation in Fig. 5(b), from which we extract single-particle energies of about 27 meV and 36 meV for e_{12} and e_{13} , respectively. As explained above, even if the second electron subband is populated, only the first heavy-hole subband will be populated with holes. Therefore, we do not expect hole excitations, starting at the second hole subband. In Fig. 7(b), the extracted intensities of the Raman lines are plotted versus the energy of the scattered light, i.e., the energy of the Raman excitations on the absolute energy scale. Corresponding to our analysis above, this should resemble the absorption of the second intermediate state of the resonant scattering process, i.e., the corresponding van Hove singularity. The black dots correspond to the e_{01} excitation. This curve resembles nicely the asymmetric shape of the $e_0 - l_0$ van Hove singularity [cf. blue curve for $\mathbf{E} \parallel \mathbf{z}$ in Fig. 6(b)]. In Fig. 7(c), the resonant scattering process for the e_{12} intersubband excitation is sketched. The relevant transition

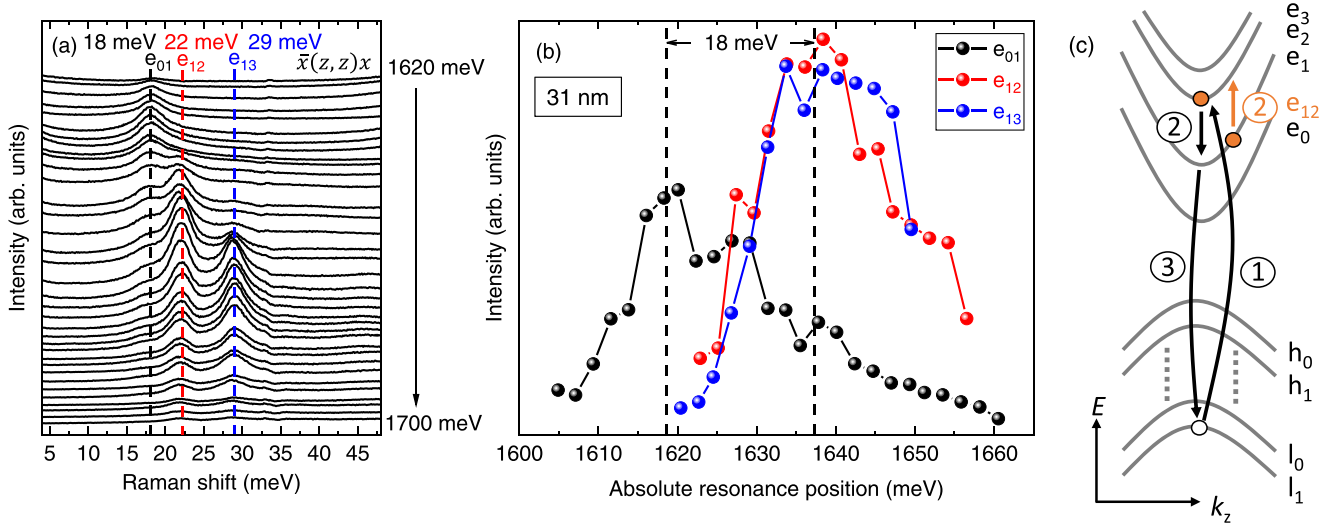


FIG. 7. (a) RILS spectra of the 31-nm wire at a laser power of 5 mW for different laser energies. (b) Intensities of the observed Raman excitations of (a) plotted versus their position on the absolute energy scale. (c) Schematic picture of the resonant scattering process, which leads to the creation of an e_{12} intersubband excitation.

in the third step would be the $e_1 \rightarrow l_1$ van Hove singularity. The same holds for the excitation of the e_{13} intersubband excitation in the same energy range. A resonance with the $e_2 \rightarrow l_2$ van Hove singularity, on the other hand, would be expected at much higher laser energies. The results for these excitations, shown in Fig. 7(b) as red and blue filled dots, confirm this interpretation. Both excitations are resonant at about the same energy, which is by about 18 meV larger than that for the e_{01} excitation. This just equals the energy of the e_{01} excitation itself, neglecting the small splitting of the light-hole band.

We note that a qualitatively similar redshift of the subband spacing e_{01} between the first and second conduction-band subbands in gated, modulation-doped GaAs-AlGaAs quantum wells was reported by Goñi *et al.* [68] and Giudici *et al.* [69], using PL and Raman experiments of the intersubband excitations. The authors observed a redshift of the subband spacing e_{01} as well as of the corresponding collective intersubband excitations, SDE and CDE, when the second subband e_1 was populated with electrons via application of a gate voltage. By comparison to calculations, employing time-dependent local-density approximation, they conclude that the redshift of e_{01} is due to exchange-correlation effects, which overcompensate the blueshift with increasing density due to the direct Coulomb interaction. In Ref. [70], Giudici *et al.* were able to investigate the density dependence of both intersubband excitations, e_{01} and e_{12} , of the gated quantum wells. They find that, while e_{01} redshifts with population of the second subband, e_{12} shows a strong blueshift. The authors argue that this happens since the third subband, e_2 , is still unoccupied; hence the direct Coulomb interaction dominates and causes the blueshift of e_{12} .

We also believe that the redshift, observed in our experiments on 1D intersubband excitations in the 31-nm wire at high illumination power, is caused by many-particle interactions in the photoexcited electron-hole plasma. However, there is a subtle difference in our results, when compared

to Refs. [68–70]. In our experiments on 1D intersubband excitations in the 31-nm wire we find that *all* observed intersubband excitations, e_{01} , e_{12} , and e_{13} , redshift when the second subband is occupied: we can get an estimate of the excitation energies e_{12} and e_{13} at low power, when only the lowest subband is significantly occupied, when we pump resonantly electrons into the second subband e_1 via the $l_1 \rightarrow e_1$ transition. Then, a nonthermal population is created in the e_1 subband. Figure 8 shows exemplarily such a measurement on the 31-nm wire. The laser energy is in the upper range

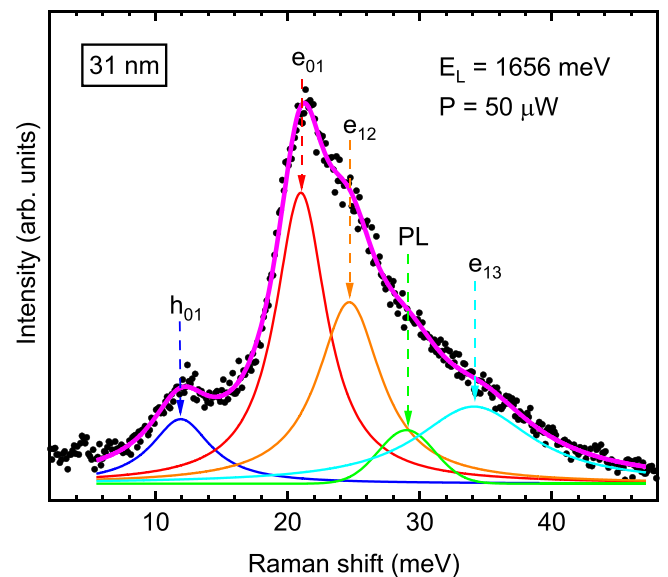


FIG. 8. Raman spectrum of the 31-nm wire, taken at a laser energy, close to the $l_1 \rightarrow e_1$ transition, where electrons are pumped resonantly into the e_1 subband. The colored lines are fits, using a set of Lorentzian lines, except for the hot PL, which is a Gaussian. The magenta line is the sum of all fit lines.

of energies used for the resonance measurement, shown in Fig. 6(b) (black and light-green dots). In such experiments we observe indications of e_{12} and e_{13} in the high-energy flank of e_{01} (see Fig. 8), which allow us to estimate their energies for the 31-nm wire. The fact that we clearly observe the intersubband hole excitation h_{01} tells us that still mainly the lowest subband is occupied, and the population in e_1 is nonthermal. From fits we find energies of ~ 21.0 meV, ~ 24.5 meV, and ~ 34.1 meV for e_{01} , e_{12} , and e_{13} at low power [compare to 20 meV, 27 meV, and 36 meV from band-structure calculations, Fig. 5(b)] and of 18 meV, 22 meV, and 29 meV at high power [cf. Fig. 7(a)]. Thus all observed 1D intersubband excitations experimentally show a redshift of about 3–5 meV when the second subband is occupied. The difference to the results in Refs. [68–70] may lie in the fact that we investigate a charge-neutral, photoexcited electron-hole plasma, while in Refs. [68–70] modulation-doped, gated quantum wells were investigated, where also band-bending effects due to space charges may play a role. Therefore, the origin of our observed redshifts is still elusive to us, though we truly believe that it has to come from many-particle interaction effects in the electron-hole plasma, which certainly need more theoretical investigations.

IV. CONCLUSION

In conclusion, we have observed intersubband excitations of photoexcited electrons and holes in ultrathin core-shell nanowires via resonant inelastic light scattering. A three-step scattering mechanism, which is based on the resonant Coulomb scattering of photoexcited electron-hole pairs by individual electrons or holes of the electron-hole plasma, can qualitatively explain the most salient features of the experiments. By the combination of the resonant Raman data, photoluminescence, and photoluminescence excitation experiments, the quantized subband structure of the nanowires is deduced, which can be nicely modeled by realistic $\mathbf{k} \cdot \mathbf{p}$ calculations.

ACKNOWLEDGMENTS

Financial support by the Deutsche Forschungsgemeinschaft (DFG, German Research Foundation), Project-ID No. 314695032, SFB 1277 (subprojects No. A01, No. B06/B05, and No. B11), and Project-ID No. 451072703 (F.D.) is gratefully acknowledged. T.K. acknowledges DFG funding via Projects No. KO3612/4-1 (Project-ID 648265) and No. KO3612/7-1 (Project-ID 679265).

-
- [1] F. Dirnberger, M. Kammermeier, J. König, M. Forsch, P. E. Faria Junior, T. Campos, J. Fabian, J. Schliemann, C. Schüller, T. Korn, P. Wenk, and D. Bougeard, *Appl. Phys. Lett.* **114**, 202101 (2019).
 - [2] N. Vainorius, S. Lehmann, A. Gustafsson, L. Samuelson, K. A. Dick, and M.-E. Pistol, *Nano Lett.* **16**, 2774 (2016).
 - [3] B. Loitsch, D. Rudolph, S. Morkötter, M. Döblinger, G. Grimaldi, L. Hanschke, S. Matich, E. Parzinger, U. Wurstbauer, G. Abstreiter, J. J. Finley, and G. Koblmüller, *Adv. Mater.* **27**, 2195 (2015).
 - [4] P. Corfdir, H. Li, O. Marquardt, G. Gao, M. R. Molas, J. K. Zettler, D. van Treeck, T. Flissikowski, M. Potemski, C. Draxl, A. Trampert, S. Fernández-Garrido, H. T. Grahn, and O. Brandt, *Nano Lett.* **18**, 247 (2018).
 - [5] C. Schüller, *Inelastic Light Scattering of Semiconductor Nanostructures, Fundamentals and Recent Advances*, Springer Tracts in Modern Physics Vol. 219 (Springer, Berlin, 2006).
 - [6] A. Pinczuk, H. L. Störmer, R. Dingle, J. M. Worlock, W. Wiegmann, and A. C. Gossard, *Solid State Commun.* **32**, 1001 (1979).
 - [7] G. Abstreiter and K. Ploog, *Phys. Rev. Lett.* **42**, 1308 (1979).
 - [8] J. S. Weiner, G. Danan, A. Pinczuk, J. Valladares, L. N. Pfeiffer, and K. W. West, *Phys. Rev. Lett.* **63**, 1641 (1989).
 - [9] T. Egeler, G. Abstreiter, G. Weimann, T. Demel, D. Heitmann, P. Grambow, and W. Schlapp, *Phys. Rev. Lett.* **65**, 1804 (1990).
 - [10] C. Schüller, G. Biese, K. Keller, C. Steinebach, D. Heitmann, P. Grambow, and K. Eberl, *Phys. Rev. B* **54**, R17304 (1996).
 - [11] G. Biese, C. Schüller, K. Keller, C. Steinebach, D. Heitmann, P. Grambow, and K. Eberl, *Phys. Rev. B* **53**, 9565 (1996).
 - [12] A. R. Goñi, A. Pinczuk, J. S. Weiner, J. M. Calleja, B. S. Dennis, L. N. Pfeiffer, and K. W. West, *Phys. Rev. Lett.* **67**, 3298 (1991).
 - [13] A. Schmeller, A. R. Goñi, A. Pinczuk, J. S. Weiner, J. M. Calleja, B. S. Dennis, L. N. Pfeiffer, and K. W. West, *Phys. Rev. B* **49**, 14778 (1994).
 - [14] C. Dahl, B. Jusserand, and B. Etienne, *Phys. Rev. B* **51**, 17211 (1995).
 - [15] A. R. Goñi, A. Pinczuk, J. S. Weiner, B. S. Dennis, L. N. Pfeiffer, and K. W. West, *Phys. Rev. Lett.* **70**, 1151 (1993).
 - [16] C. Steinebach, R. Krahne, G. Biese, C. Schüller, D. Heitmann, and K. Eberl, *Phys. Rev. B* **54**, R14281 (1996).
 - [17] E. Ulrichs, G. Biese, C. Steinebach, C. Schüller, D. Heitmann, and K. Eberl, *Phys. Rev. B* **56**, R12760 (1997).
 - [18] F. Perez, S. Zanier, S. Hameau, B. Jusserand, Y. Guldner, A. Cavanna, L. Ferlazzo-Manin, and B. Etienne, *Appl. Phys. Lett.* **72**, 1368 (1998).
 - [19] M.-T. Bootsmann, C.-M. Hu, Ch. Heyn, D. Heitmann, and C. Schüller, *Phys. Rev. B* **67**, 121309(R) (2003).
 - [20] R. Strenz, U. Bockelmann, F. Hirler, G. Abstreiter, G. Böhm, and G. Weimann, *Phys. Rev. Lett.* **73**, 3022 (1994).
 - [21] D. J. Lockwood, P. Hawrylak, P. D. Wang, C. M. Sotomayor Torres, A. Pinczuk, and B. S. Dennis, *Phys. Rev. Lett.* **77**, 354 (1996).
 - [22] C. Schüller, K. Keller, G. Biese, E. Ulrichs, L. Rolf, C. Steinebach, D. Heitmann, and K. Eberl, *Phys. Rev. Lett.* **80**, 2673 (1998).
 - [23] T. Brocke, M.-T. Bootsmann, M. Tews, B. Wunsch, D. Pfannkuche, Ch. Heyn, W. Hansen, D. Heitmann, and C. Schüller, *Phys. Rev. Lett.* **91**, 257401 (2003).
 - [24] T. Köppen, D. Franz, A. Schramm, Ch. Heyn, D. Heitmann, and T. Kipp, *Phys. Rev. Lett.* **103**, 037402 (2009).
 - [25] D. Hamilton and A. L. McWhorter, in *Light Scattering Spectra of Solids*, edited by G. B. Wright (Springer, New York, 1969), p. 309.

- [26] A. Pinczuk, S. Schmitt–Rink, G. Danan, J. P. Valladares, L. N. Pfeiffer, and K. W. West, *Phys. Rev. Lett.* **63**, 1633 (1989).
- [27] C. Steinebach, C. Schüller, and D. Heitmann, *Phys. Rev. B* **59**, 10240 (1999).
- [28] S. Das Sarma and D.-W. Wang, *Phys. Rev. Lett.* **83**, 816 (1999).
- [29] B. Jusserand, M. N. Vijayaraghavan, F. Laruelle, A. Cavanna, and B. Etienne, *Phys. Rev. Lett.* **85**, 5400 (2000).
- [30] C. Steinebach, C. Schüller, and D. Heitmann, *Phys. Rev. B* **61**, 15600 (2000).
- [31] C. Schüller, C. Steinebach, and D. Heitmann, *Solid State Commun.* **119**, 323 (2001).
- [32] B. Ketterer, M. Heiss, E. Uccelli, J. Arbiol, and A. Fontcuberta I Morral, *ACS Nano* **5**, 7585 (2011).
- [33] B. Ketterer, M. Heiss, M. J. Livrozet, A. Rudolph, E. Reiger, and A. Fontcuberta i Morral, *Phys. Rev. B* **83**, 125307 (2011).
- [34] O. Demichel, M. Heiss, J. Bleuse, M. Mariette, A. Fontcuberta, and I. Morral, *Appl. Phys. Lett.* **97**, 201907 (2010).
- [35] W. Peng, F. Jabeen, B. Jusserand, J. C. Harmand, and M. Bernard, *Appl. Phys. Lett.* **100**, 073102 (2012).
- [36] P. Kusch, S. Breuer, M. Ramsteiner, L. Geelhaar, H. Riechert, and S. Reich, *Phys. Rev. B* **86**, 075317 (2012).
- [37] S. Furthmeier, F. Dirnberger, J. Hubmann, B. Bauer, T. Korn, C. Schüller, J. Zweck, E. Reiger, and D. Bougeard, *Appl. Phys. Lett.* **105**, 222109 (2014).
- [38] S. Furthmeier, F. Dirnberger, M. Gmitra, A. Bayer, M. Forsch, J. Hubmann, C. Schüller, E. Reiger, J. Fabian, T. Korn, and D. Bougeard, *Nat. Commun.* **7**, 12413 (2016).
- [39] S. Das Sarma and D. W. Wang, *Phys. Rev. Lett.* **84**, 2010 (2000).
- [40] G. Bastard, *Phys. Rev. B* **24**, 5693 (1981).
- [41] G. A. Baraff and D. Gershoni, *Phys. Rev. B* **43**, 4011 (1991).
- [42] M. G. Burt, *J. Phys.: Condens. Matter* **4**, 6651 (1992).
- [43] G. Bastard, *Wave Mechanics Applied to Semiconductor Heterostructures* (Les Éditions de Physique, Les Ulis, France, 1988).
- [44] G. M. Sipahi, R. Enderlein, L. M. R. Scolfaro, and J. R. Leite, *Phys. Rev. B* **53**, 9930 (1996).
- [45] N. Vukmirović and S. Tomić, *J. Appl. Phys.* **103**, 103718 (2008).
- [46] M. Ehrhardt and T. Koprucki, *Multi-band Effective Mass Approximations: Advanced Mathematical Models and Numerical Techniques* (Springer, Berlin, 2014), Vol. 94.
- [47] J. A. Budagosky, *Phys. Rev. B* **96**, 115443 (2017).
- [48] S. L. Chuang and C. S. Chang, *Phys. Rev. B* **54**, 2491 (1996).
- [49] T. Cheiwchanamngij and W. R. Lambrecht, *Phys. Rev. B* **84**, 035203 (2011).
- [50] P. E. Faria Junior, T. Campos, C. M. O. Bastos, M. Gmitra, J. Fabian, and G. M. Sipahi, *Phys. Rev. B* **93**, 235204 (2016).
- [51] T. Campos, P. E. Faria Junior, M. Gmitra, G. M. Sipahi, and J. Fabian, *Phys. Rev. B* **97**, 245402 (2018).
- [52] S. L. Chuang, *Physics of Optoelectronic Devices* (John Wiley, New York, 1995).
- [53] P. E. Faria Junior, G. Xu, Y.-F. Chen, G. M. Sipahi, and I. Žutić, *Phys. Rev. B* **95**, 115301 (2017).
- [54] P. E. Faria Junior, D. Tedeschi, M. De Luca, B. Scharf, A. Polimeni, and J. Fabian, *Phys. Rev. B* **99**, 195205 (2019).
- [55] B. Zhang, Z. Nie, B. Wang, D. Wang, J. Tang, X. Wang, J. Zhang, G. Xing, W. Zhang, and Z. Wei, *Phys. Chem. Chem. Phys.* **22**, 25819 (2020).
- [56] G. Danan, A. Pinczuk, J. P. Valladares, L. N. Pfeiffer, K. W. West, and C. W. Tu, *Phys. Rev. B* **39**, 5512 (1989).
- [57] A. O. Govorov, *J. Phys.: Condens. Matter* **9**, 4681 (1997).
- [58] Y. Hu, S. Chen, X. Cong, S. Sun, J.-b. Wu, D. Zhang, F. Yang, J. Yang, P.-H. Tan, and Y. Li, *J. Phys. Chem. Lett.* **11**, 10497 (2020).
- [59] F. Dirnberger, D. Abujetas, J. König, M. Forsch, T. Koller, I. Gronwald, C. Lange, R. Huber, C. Schüller, T. Korn, J. Sanchez-Gil, and D. Bougeard, *Nano Lett.* **19**, 7287 (2019).
- [60] This is also supported by the comparison of the resonance widths of the intersubband excitations of the 25-nm and 31-nm wire in Figs. 6(a) and 6(b) (black and light-green dots): also there, the resonances in the 31-nm wire are narrower than those in the 25-nm wire.
- [61] A. Mooradian and G. B. Wright, *Phys. Rev. Lett.* **16**, 999 (1966).
- [62] J. Yan, Y. Zhang, P. Kim, and A. Pinczuk, *Phys. Rev. Lett.* **98**, 166802 (2007).
- [63] A. De and C. E. Pryor, *Phys. Rev. B* **81**, 155210 (2010).
- [64] F. Bechstedt and A. Belabbes, *J. Phys.: Condens. Matter* **25**, 273201 (2013).
- [65] M. Gmitra and J. Fabian, *Phys. Rev. B* **94**, 165202 (2016).
- [66] N. Vainorius, S. Kubitza, S. Lehmann, L. Samuelson, K. A. Dick, and M.-E. Pistol, *Nanoscale* **10**, 1481 (2018).
- [67] M. De Luca, G. Lavenuta, A. Polimeni, S. Rubini, V. Grillo, F. Mura, A. Miriametro, M. Capizzi, and F. Martelli, *Phys. Rev. B* **87**, 235304 (2013).
- [68] A. R. Goñi, U. Haboeck, C. Thomsen, K. Eberl, F. A. Reboredo, C. R. Proetto, and F. Guinea, *Phys. Rev. B* **65**, 121313(R) (2002).
- [69] P. Giudici, A. R. Goñi, C. Thomsen, P. G. Bolcatto, C. R. Proetto, and K. Eberl, *Phys. Rev. B* **70**, 235418 (2004).
- [70] P. Giudici, A. R. Goñi, P. G. Bolcatto, C. R. Proetto, C. Thomsen, K. Eberl, and M. Hauser, *Europhys. Lett.* **77**, 37003 (2007).